

Precipitation Behaviors of AlN Inclusion in High-Al Steel



YUHANG GUO, LEI CAO, GUOCHENG WANG, and CHUNWEI LIU

High-Al steel was prepared under laboratory conditions. The single-particle AlN and multi-particle aggregated AlN, AlON, AlN–MnS, and Al₂O₃–AlN–MnS inclusions were observed by FESEM-EDS. The single-particle AlN inclusions are mainly in the form of blocks and strips, with their size mainly concentrated in the range of 1 to 5 μm. The aggregated AlN inclusions are polygonal, toroidal, and irregular in shape and their size mainly concentrated in the range of 1 to 13 μm. The size of AlN–MnS and Al₂O₃–AlN–MnS inclusions is less than 15 μm. Thermodynamic calculation shows that AlN inclusion precipitates in the two-phase region. Growth kinetics showed that the size of AlN inclusions at the end of solidification ranged from 1 to 7 μm, which is consistent with the observed size of single-particle AlN inclusions. Lattice mismatch indicates that AlN can be as an effective site for MnS nucleation. The equilibrium constant $\log K_{\text{AlON}} = -137841.3/T + 45.49$ of AlON inclusions is constructed. Furthermore, the mass percentage changes of inclusions during solidification were predicted based on the microsegregation model combined with the FactSage software.

<https://doi.org/10.1007/s11663-022-02688-y>

© The Minerals, Metals & Materials Society and ASM International 2022

I. INTRODUCTION

IN recent years, with the advancement of science and technology and modern industry, the demand for high-quality steel for automobile production has been increasing. Due to the needs of environmental protection and energy saving, the lightweight of automobiles has become the key direction of the world's automobile development. In automotive applications, the combination of light weight and ultra-high strength makes these steels more attractive than traditional steels, and therefore, they have received extensive attention from many scholars.^[1–4] However, in high-Al steels, high aluminum content can cause many problems in the steelmaking and casting process. With the increase of Al content in steel, the chemical, type, size, composition, and morphology of non-metallic inclusions are different from regular Al-killed steel.

Some researchers^[5–10] have found that the main inclusion in high-Al steel is AlN, and the precipitation of AlN in high-Al steel is much easier than that in regular Al-killed steel. Alba *et al.*^[11] studied the effect of Mn content on inclusion characteristics in Fe–xMn–3Al steel ($x = 2, 5, 20$) and found that with the increase of manganese content (2 to 20 pct), the total amount of inclusions increased 4 to 8 times, mainly due to the increase of AlN and MnS. In addition, changes in Mn content lead to changes in the solubility of N in the steel. Peak *et al.*^[12] found that Mn significantly increased the solubility of N in liquid Fe–Mn and Fe–Mn–Al alloys. Therefore, the formation of AlN inclusions will be promoted in steels with higher Mn content.

Kang *et al.*^[13] and Funnell *et al.*^[14] show that during the rolling process, AlN inclusions will lead to deterioration of the thermoplasticity of the steel. Croft *et al.*^[15] found that AlN inclusions precipitated at the end of solidification in Al-killed steel (Al content of 0.17 pct). Shi *et al.*^[16] found that AlN inclusions in high-Al steel (with Al content of 1 pct) also precipitated at the solidification front during electroslag remelting. Based on thermodynamic calculations, Zhuang *et al.*^[5] showed that the precipitation of AlN inclusions in Fe–25Mn–3Si–3Al steel is different from most high-Al steels or Al-killed steels, and AlN inclusions are precipitated in the liquid phase. Liu *et al.*^[17] found that AlN of TWIP steel (Al content 3 pct) was precipitated in the liquid phase in AOD (N content 24 ppm), while AlN was precipitated in the solidification process in ESR (N content 6 ppm). And through calculation, it was found

YUHANG GUO, LEI CAO, and GUOCHENG WANG are with the School of Materials and Metallurgy, University of Science and Technology Liaoning, Anshan 114051, Liaoning, P.R. China. CHUNWEI LIU is with the Technology Center, Shandong Iron and Steel Company Ltd. Laiwu Company, Laiwu, 271100, P.R. China. Contact e-mail: wang_guocheng@163.com

Manuscript submitted September 7, 2022; accepted October 30, 2022.

Article published online November 23, 2022.

that only 10 ppm of N content can form AlN. Wang *et al.*^[18] found that the size of AlN can be controlled under the condition of high cooling rate during solidification. Nabeel *et al.*^[19] found that the precipitation rate of MnS on AlN, AlON (Al₂O₃ + AlN), and Al₂O₃ inclusions is related to the mismatch rate, and the order of the precipitation rate is AlN > AlON (Al₂O₃ + AlN) > Al₂O₃. At present, the precipitation regular of AlN and its complex inclusions is still unclear. Therefore, it is necessary to analyze the formation mechanism of AlN inclusions in high-Al steel to provide a theoretical basis for the control of inclusions in the smelting process of high-Al steel.

In this paper, the morphology and composition of AlN and its complex inclusions in high-Al steel were observed. According to the experimental steel component, the thermodynamics and kinetics of single-particle AlN precipitation during the solidification process were calculated. In addition, the formation mechanism of AlN–MnS and AlON inclusions was discussed.

II. EXPERIMENTAL

A. Materials and Processes

The raw material of steel includes pure iron powder 700 g, Fe–Mn alloy 60 g, Fe–Si alloy 10 g, ferrous oxalate 1.575 g, (99 mass pct), and high-purity aluminum wire 8.75 g (99.99 mass pct Al). The compositions of raw materials containing pure iron, Fe–Mn alloy, Fe–Si alloy, and Al wires are shown in Table I.

A tubular resistance furnace was used to smelt and deoxidize for molten steel. Figure 1 shows a high-temperature tubular resistance furnace. The furnace temperature is controlled by an automatic temperature controller, and the furnace temperature is monitored in real time with a double platinum and rhodium thermocouple. First, the pure iron powder and ferrous oxalate were put into an alumina crucible (oxygen content was almost 200 ppm added to the melt), and then the alumina crucible was put into a tubular resistance furnace. The temperature was raised to 1873 K (1600 °C) and held for 60 min to ensure complete melting of the pure iron in the crucible. Then, Fe–Mn alloy, Fe–Si alloy, and aluminum wire wrapped with high-purity iron sheet were added to the melt in sequence, and then the temperature was cooled by cooling in the furnace. The high-purity argon gas was used for protection in the whole process, and the gas flow rate of 1 L/min. When the furnace body was cooled to room temperature, take out the sample, and cut the metallographic sample with an electric spark cutting machine.

B. Sample Analysis Method

The chemical compositions of the steel samples were analyzed by the chemical methods. The total oxygen (T.O) content and total nitrogen (T.N) content in the steel were measured using a nitrogen–oxygen analyzer

Table I. Chemical Composition of Raw Materials (Mass Percent)

Type	C	Si	Mn	P	S	Al
Pure Iron	< 0.005	0.01	0.046	0.0032	0.013	
Fe–Mn Al-loy	5.7	2.3	65.03	0.21	0.03	
Fe–Si Al-loy	0.2	72.02			0.02	1
Al Wire						99.99

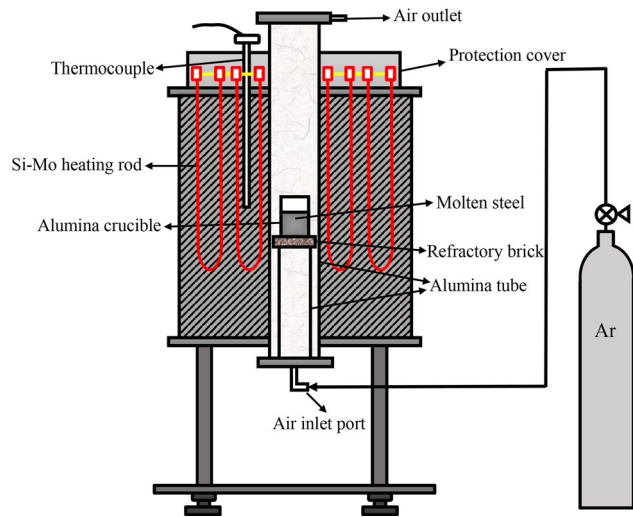


Fig. 1—Schematic diagram of MoSi₂ high-temperature tubular resistance furnace.

(model: TC600). The content of the carbon and sulfur was measured by the carbon–sulfur analyzer. The content of manganese, aluminum, and other elements was analyzed by inductively coupled plasma atomic emission spectrometry (ICP-AES). Table II shows the chemical composition of the experimental steel samples.

An electric spark cutting machine is used to cut the solidified sample into two cylinders as shown in Figure 2(a). The upper half is taken and a cuboid is cut out at the center as shown in Figure 2(b), and the cuboid is cut according to Figure 2(c) and cut into two 10 × 10 × 12 mm rectangular parallelepipeds, and then metallographic sandpaper (60 mesh–2000 mesh) and diamond polishing paste is used to polish one of the samples into a mirror surface as a scanning electron microscope observation sample, as shown in Figure 2(d).

A field emission scanning electron microscope (FESEM, model: ZEISS ΣIGMA HD) combined with an energy-dispersive spectrometer (EDS, model: Oxford-X-Max 50 mm²) was used to analyze the composition and morphological distribution of inclusions in the sample.

Table II. Sample Component Test Results (Mass Percent)

Elements	C	Si	Mn	P	S	T.O	T.N	Al
Content	0.32	0.94	4.55	0.019	0.011	0.0005	0.00214	0.86

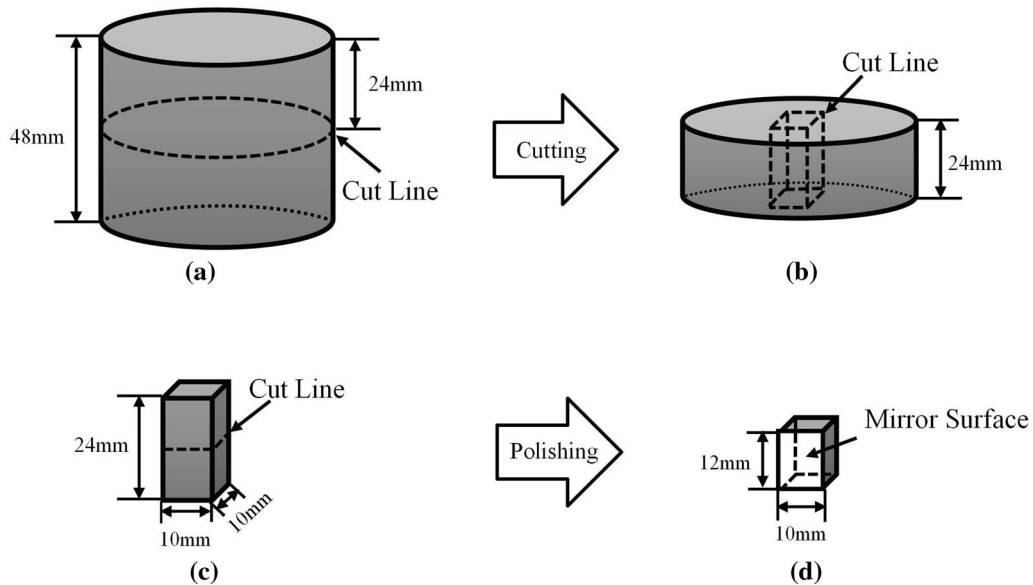


Fig. 2—Sample preparation process. (a) through (c) Metallographic sample-cutting process; (d) metallographic sample-polishing process.

III. RESULTS

A. Observation of AlN Inclusions

Figure 3 shows the morphology and element mapping results of single and multi-particle AlN inclusions observed by FESEM-EDS. Figures 3(a) and (b) shows single-particle AlN inclusions. These inclusions are mainly lump shaped and strip shaped in steel with sizes less than $5\ \mu\text{m}$. Figures 3(c) through (h) shows AlN with multi-particle aggregation state. Through the observation of the picture, it can be found that the multi-particle aggregation state AlN is composed of multiple single-particle AlN with small size, mainly in multilateral shape, ring shape, and irregular shape, and its size is between 1 and $12\ \mu\text{m}$. As shown in Figure 3(c), it is composed of three polygons AlN which are connected by angular opposite side and side to side. In Figure 3(d), there are annular AlN inclusions in the middle and multiple irregular small-size AlN inclusions around. In Figure 3(e), it is composed of multiple polygonal AlN inclusions which are closely connected with edges. In Figure 3(f), the AlN inclusions of two polygons are adjacent to a strip AlN inclusion in the upper right and are connected with the corner of a pentagonal AlN inclusion in the upper left. In Figure 3(g), there are two irregular AlN inclusions on both sides, and two spherical and irregular AlN inclusions above. In Figure 3(h),

there are four polygonal AlN inclusions, and they are combined in the same way as in Figure 3(e), all of which are closely combined with each other.

B. Observation of AlN Complex Inclusions

Figure 4 shows the morphology and composition of the AlON inclusions observed in the experimental steel. In Figures 4(a) through (c), the AlON inclusions are irregular and trapezoidal, with sizes less than $3\ \mu\text{m}$. Figure 5 shows the AlN–MnS complex inclusions in steel. In Figure 5(a), MnS precipitates on the surface of AlN in a point-like shape with a small size, while AlN inclusions are formed by the aggregation of two single-particle AlN inclusions with a total length of about $8\ \mu\text{m}$. In Figure 5(b), the long strips of MnS are precipitated around AlN, and the size of MnS is large, $13\ \mu\text{m}$. The AlN on the right is sickle shaped, and the upper and lower parts are both smaller than $4\ \mu\text{m}$.

Figure 6 shows the Al_2O_3 –AlN–MnS complex inclusions in the steel, and the elements mapping results are those of Figures 6(b) and (d). In Figure 6(a), there are three elliptic and irregular Al_2O_3 . The outermost strip AlN is wrapped on the surface of Al_2O_3 , followed by MnS located in the center, which wraps on the surface of Al_2O_3 and AlN and acts as a connection, with a larger size of $14\ \mu\text{m}$. In Figure 6(b) through (d), the core parts are all spherical or elliptical Al_2O_3 inclusions, followed

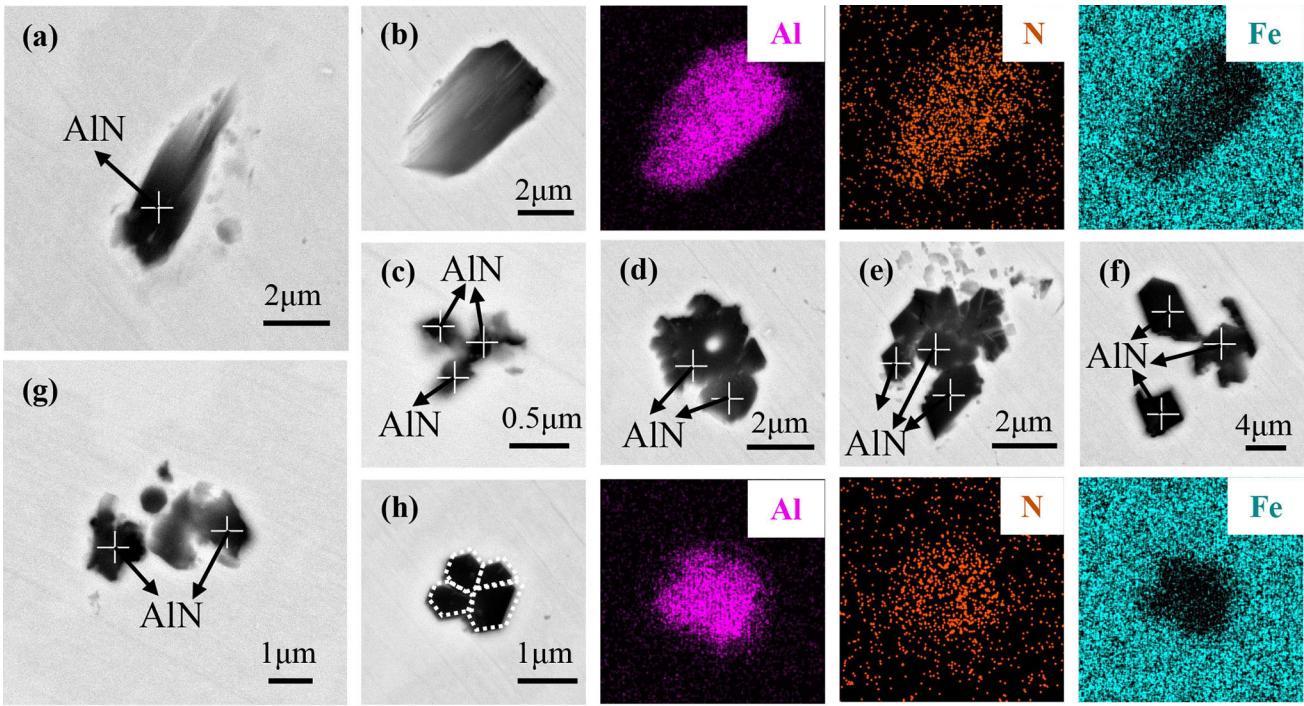


Fig. 3—The morphology and elements mapping of single-particle and multi-particle AlN inclusions. (a) and (b) are single-particle AlN inclusions; (c) through (h) are multi-particle-aggregated AlN inclusions.

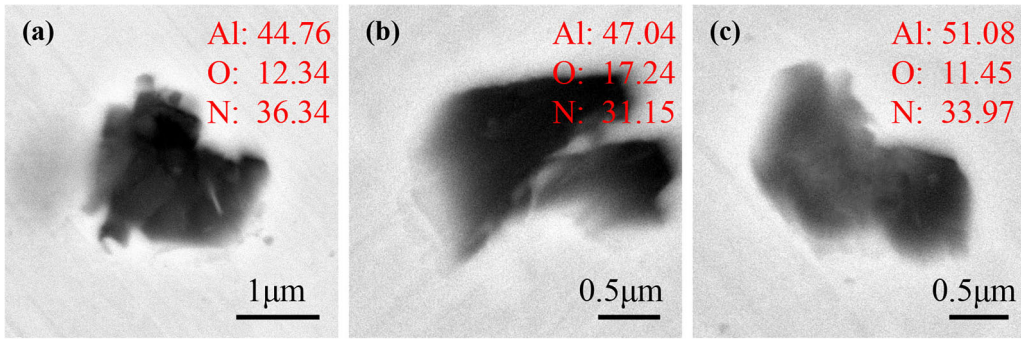


Fig. 4—The morphology and composition of AlON inclusions. (a) and (c) are irregular AlON inclusions; (b) is trapezoidal AlON inclusions.

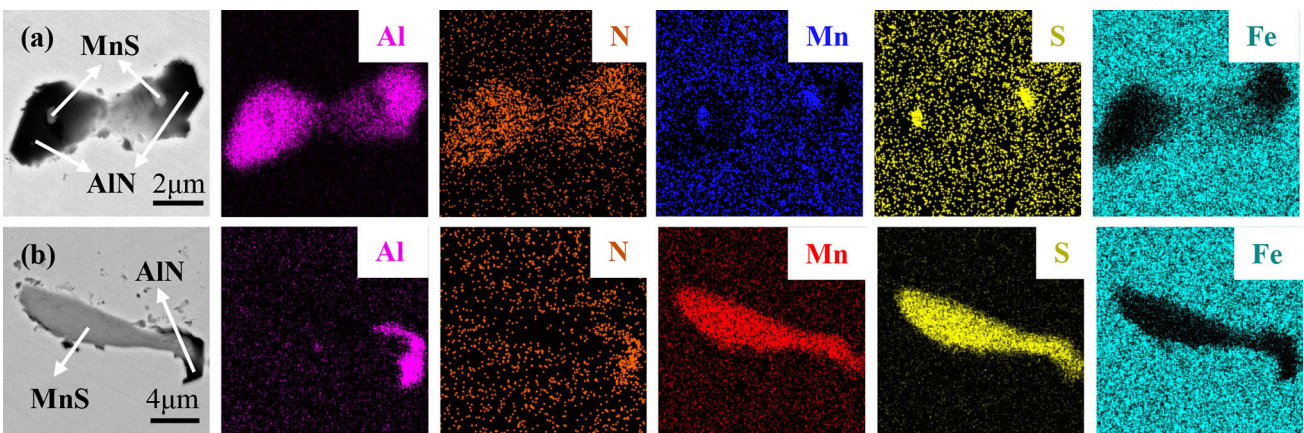


Fig. 5—The morphology and elements mapping of AlN-MnS inclusions. (a) is dumbbell-shaped AlN-MnS inclusions; (b) is long strip of AlN-MnS inclusions.

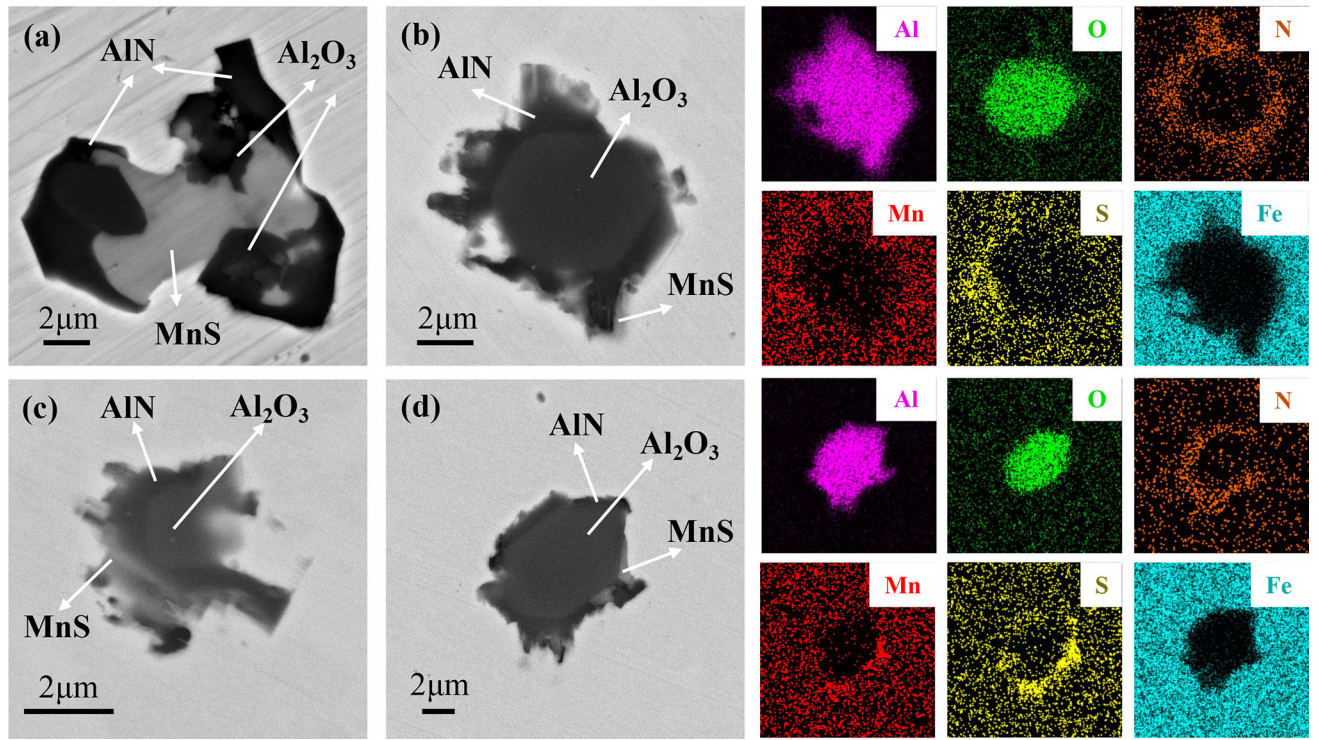


Fig. 6—The morphology and elements mapping of Al_2O_3 -AlN-MnS inclusions. (a) is an Al_2O_3 -AlN-MnS inclusions formed by the link of MnS; (b) through (d) are with Al_2O_3 inclusions as the core, followed by AlN inclusions and MnS inclusions in the outermost layer.

by AlN inclusions, and the outermost layer is MnS inclusions, and the size of the inclusions is 5 to 10 μm . In Figures 6(b) and (d), AlN inclusions are wrapped around Al_2O_3 inclusions, MnS inclusions are wrapped around AlN inclusions, and in Figure 6(c), AlN inclusions are wrapped around Al_2O_3 inclusions. The left side of the inclusions, followed by the MnS inclusions, are also wrapped around the left side of the AlN inclusions.

C. Inclusions Particles Size Distribution

Using the automatic statistical analysis system for inclusions, the particle size distribution of non-metallic inclusions in the experimental steel was counted, and the results are shown in Figure 7. As can be seen from the figures, the sizes of single-particle AlN inclusions are mainly 1 to 5 μm , the sizes of multi-particle aggregated AlN inclusions are mainly 1 to 13 μm , the sizes of AlN-MnS inclusions are mainly 5 to 10 μm , and the sizes of Al_2O_3 -AlN-MnS inclusions are mainly 5 to 15 μm .

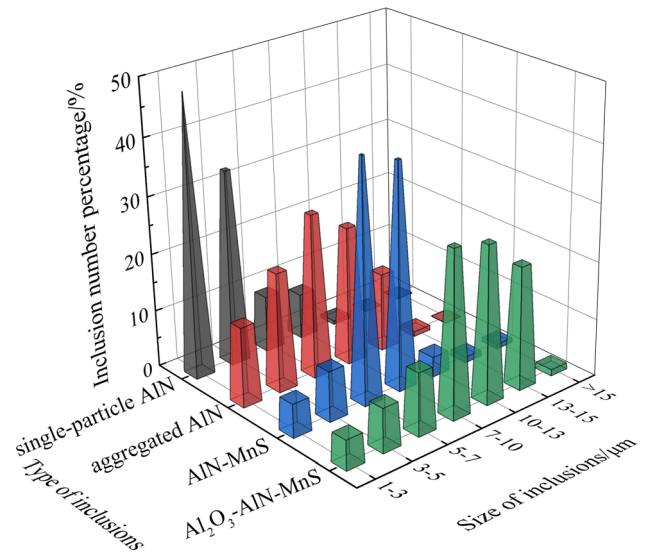
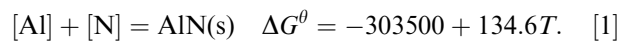


Fig. 7—Size distribution of inclusions in experimental steels.

IV. DISCUSSION

A. Thermodynamics Precipitation of AlN Inclusions

At 1873 K, the chemical reaction formula formed by AlN is^[20]



The equilibrium constant of the reaction can be expressed as follows:

$$K_{\text{AlN}}^E = \frac{a_{\text{AlN}}}{a_{\text{Al}} \cdot a_{\text{N}}} = \frac{a_{\text{AlN}}}{f_{\text{Al}}[\text{pct Al}]f_{\text{N}}[\text{pct N}]}, \quad [2]$$

where ΔG^θ presents the standard Gibbs free energy for the formation of AlN inclusions in molten steel, K_{AlN}^E is the equilibrium constant of the reaction, a_{AlN} , a_{Al} , and a_{N} respectively represent the activity of AlN, Al, and N in steel, f_{Al} and f_{N} respectively represent the

Table III. The First-Order Interaction Coefficient Used in This Work (1873 K)^[12,21–25]

e'_i	C	Si	Mn	P	S	N	O	Al
Al	0.091	0.009	0	0.05	0.03	0.033	− 1.979	0.045
N	0.13	0.048	− 0.023	0.059	0.007	0	0.05	0.017
Mn	0.045	− 0.0327	0	− 0.06	− 0.048	− 0.091	− 0.083	—
S	0.111	0.075	− 0.026	0.035	− 0.046	− 0.072	0.01	0.041
O	− 0.45	− 0.131	− 0.021	0.07	− 0.133	0.057	− 0.2	− 3.9

activity coefficients of Al and N in steel, [pct Al] and [pct N] respectively represent the mass percentage of Al and N in the steel.

In Eq. [2], when $a_{AlN} = 1$, both sides take the logarithm of 10 at the same time, and Eq. [2] can be simplified to Eq. [3]:

$$\log K_{AlN} = -\log f_{Al} - \log[\text{pct Al}] - \log f_N - \log[\text{pct N}]. \quad [3]$$

The f_{Al} and f_N can be expressed by Eq. [4]:

$$\log f_i = \sum_j e'_j \cdot [\text{pct } j] \quad i = \text{Al, N}; \quad [4]$$

$$j = \text{C, Mn, P, S, N, O, Al},$$

where e'_i is the first-order interaction coefficient, and [pct j] is the content of each element in the steel.

Table III shows the first-order interaction coefficients of each element at 1873 K.^[12,21–25] From this, the first-order interaction coefficients are used to calculate the activity coefficients of Al and N, and the results are $\log f_{Al} = 0.077$ and $\log f_N = -0.002$. Based on the above results, Eq. [5] can be obtained:

$$\log K'_{AlN} = \log([\text{pct Al}] \cdot [\text{pct N}]) = -\frac{15850.93}{T} + 6.96 \quad [5]$$

Using FactSage 7.2 software calculations, the solidus and liquidus temperatures of steel are 1784 K and 1693 K (1511 °C and 1420 °C). According to Eqs. [1] and [2], the stability diagram of AlN formed under different temperature conditions can be obtained, as shown in Figure 8. Figure 8 shows that in this study, the composition of the steel is below the solidus temperature, indicating that AlN cannot be precipitated in the liquid phase or between the solid liquidus according to the equilibrium calculation. However, during the solidification process, Al and N elements in the molten steel undergo microscopic segregation at the solidification front, which makes the concentration of Al and N increase continuously and exceed the equilibrium value, thus increasing the driving force for the formation of AlN and leading to the precipitation of AlN in the solidification process. Therefore, the precipitation behavior of AlN during solidification is further discussed.

According to the Clyne–Kurz model,^[26] the actual mass percentage of Al and N during the solidification of molten steel are calculated:

$$C_L = C_0 [1 - (1 - 2\Omega k)x_s]^{\frac{(k-1)}{(1-2\Omega k)}}. \quad [6]$$

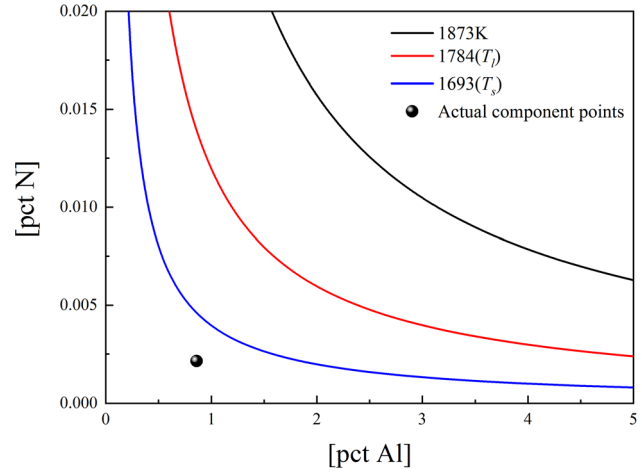


Fig. 8—Stability diagram of AlN formed under different temperature equilibrium conditions.

In Eq. [6], C_L represents the actual mass percentage of the solute element during the solidification process; C_0 represents the initial mass percentage of solute elements in molten steel; k is the distribution coefficient; x_s is the solidification fraction; Ω is the inverse diffusion coefficient, which can be expressed by Eq. [7]:

$$\Omega = \alpha \left[1 - \exp\left(-\frac{1}{\alpha}\right) \right] - \frac{1}{2} \exp\left(-\frac{1}{2\alpha}\right). \quad [7]$$

In Eq. [7], α is the Fourier number of the solute element, which can be expressed by Eq. [8]:

$$\alpha = \frac{D_s t_f}{(0.5\lambda_s)^2}. \quad [8]$$

In Eq. [8], D_s is the diffusion coefficient in the solid phase (cm^2/s); t_f is the local solidification time (s); λ_s is the distance between the secondary dendrite arms (cm). Among them, t_f and λ_s can be expressed by Eqs. [9] and [10] respectively:

$$t_f = \frac{T_l - T_s}{C_R}, \quad [9]$$

$$\lambda_s = 143.9 C_R^{-0.3616} [\text{pct C}]^{(0.5501 - 1.996[\text{pct C}])}, [\text{pct C}] > 0.15. \quad [10]$$

In Eq. [9], T_1 and T_s are the liquidus temperature and solidus temperature of steel, respectively, and C_R is the cooling rate (K/s); In Eq. [10], [pct C] is the mass percentage of carbon in the steel; λ_s is the distance between the secondary dendrite arms (cm).

Table IV shows the equilibrium distribution coefficient and diffusion coefficient of solute elements.^[27,28] According to Eq. [6], the segregation ratio of solute elements in the solidification process of steel can be obtained, as shown in Figure 9. It can be found that the changes of S and O elements are significant with the increase of solidification fraction, while the changes of Mn, Al, and N are not obvious. Figure 10 shows the changes of actual concentrations of aluminum and nitrogen at different cooling rates during the solidification process. It is found that with the increase of cooling rate, the actual concentration of Al in the residual liquid phase increases when the solidification fraction is greater than 0.5, while the actual concentration of N is basically unchanged.

At the solidification front, the actual solubility product of Al and N can be expressed by Q_{AIN} :

$$Q_{AIN} = C_{L,Al} \cdot C_{L,N}. \quad [11]$$

Table IV. The Equilibrium Distribution Coefficient and Diffusion Coefficient of Solute Elements ($R = 8,314$)^[27,28]

Element	Equilibrium Partition Coefficient(k)	Diffusion Coefficient (cm^2/s) (D)
Al	0.6	$5.9\exp(-241,417/RT)$
N	0.25	$0.008\exp(-79,078/RT)$
Mn	0.77	$0.76\exp(-224,430/RT)$
S	0.05	$4.56\exp(-214,639/RT)$
O	0.03	$0.0371\exp(-9644/RT)$

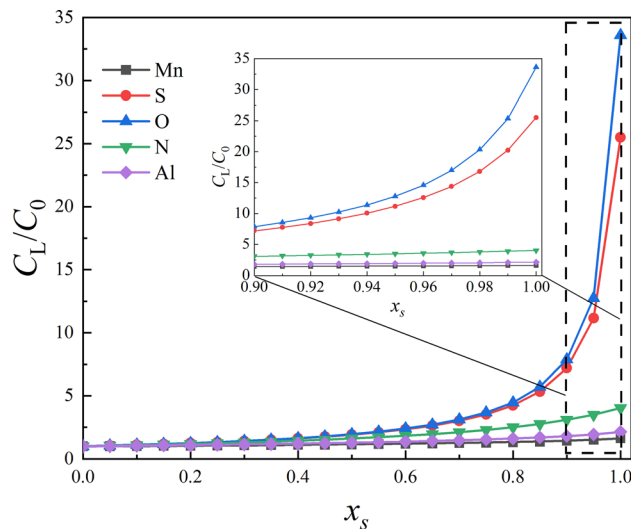


Fig. 9—Variations of concentrations of the different solute elements during solidification.

The relationship between the solidification fraction of molten steel and the temperature can be expressed by Eq. [12]:^[29]

$$T = T_0 - \frac{T_0 - T_1}{1 - x_s(T_1 - T_s)/(T_0 - T_s)}. \quad [12]$$

In Eq. [12], T is the temperature of liquid steel during solidification (K); T_0 , T_1 , and T_s are the melting temperatures of pure iron (1809 K), liquidus temperature (1784 K), and solid-phase line temperature (1693 K), respectively.

According to Eqs. [5] and [11], the relationship between $\log K'_{AIN}$, $\log Q_{AIN}$ and T and x_s can be obtained. As shown in Figure 11, AlN precipitates when the solidification fraction is about 0.79, and the corresponding precipitation temperature is about 1744 K, which is between liquidus temperature (1784 K) and solid-phase temperature (1693 K), indicating that AlN precipitates in the solidification process. It can be found from Figure 11 that as the cooling rate increases, the intersection point of $\log K'_{AIN}$, and $\log Q_{AIN}$ moves toward the direction of decreasing solid fraction, that is, AlN inclusions are more likely to form at lower solid fraction.

For multi-particle-aggregated AlN inclusions, Cao *et al.*^[30] and Sasai *et al.*^[31] have demonstrated that cavity bridging forces in MgAl_2O_4 - and Al_2O_3 -aggregated inclusions are much larger than vander Waals and capillary forces. Wang *et al.*^[32] and Liu *et al.*^[33] observed aggregated AlN inclusions by scanning electron microscopy and high-temperature confocal microscopy, and Wang *et al.*^[32] also demonstrated the dominant role of cavity-bridging forces in aggregated inclusions by calculating the forces between AlN inclusions. Therefore, in this study, it is believed that AlN inclusions begin to precipitate during the solidification process, and the single-particle AlN inclusions aggregate due to the effect of cavity bridge force.

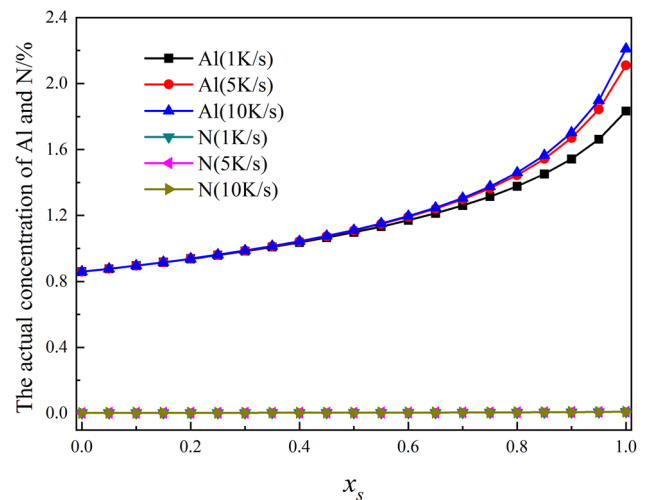


Fig. 10—Variations of actual concentrations of aluminum and nitrogen during the solidification.

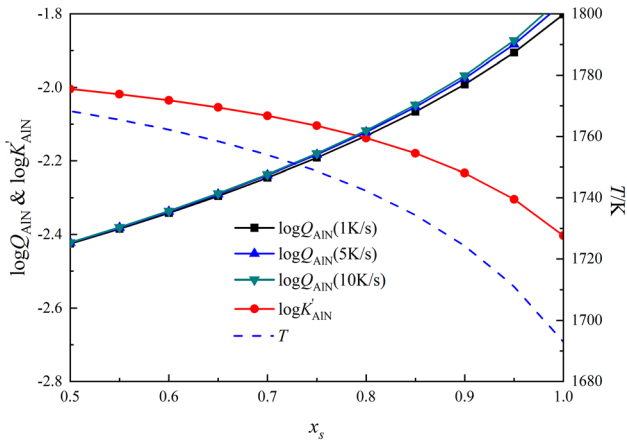


Fig. 11—Precipitation of AlN inclusions during solidification at different cooling rates.

B. Growth Kinetic of AlN Inclusions

During the solidification process, the degree of supersaturation can be expressed by the Eq. [13]. From the above, the degree of supersaturation is $S^* \geq 1$. According to the critical nucleation Eq. [14], the nucleation of AlN inclusions depends on the degree of subcooling, and the degree of subcooling depends on the local cooling rate, as shown in Eq. [15]^[34]:

$$S^* = Q_{\text{AlN}}/K'_{\text{AlN}}, \quad [13]$$

$$\Delta G^* = \frac{16\pi\sigma^3 T_1^2 f(\theta)}{3L_m^2 \Delta T^2}, \quad [14]$$

$$\frac{dT}{dR_c} = \frac{1}{1 + \frac{Af(\theta)\sigma^3 T_1^2}{\Delta H_V^2 \kappa} \cdot \frac{2T_1 - 3\Delta T}{\Delta T^2 (T_1 - \Delta T)}} \cdot \frac{\Delta T}{R_c}. \quad [15]$$

In Eq. [13], S^* is the degree of supersaturation, Q_{AlN} and K'_{AlN} are the actual solubility product and theoretical solubility product of AlN, respectively. In Eq. [14], ΔG^* is the critical nucleation work (J/mol), ΔT is the degree of subcooling (K), σ is the interfacial energy between inclusions and molten steel (J/cm²), T_1 is the liquidus temperature, $f(\theta)$ is the catalytic index, θ is the critical contact angle (deg), and L_m is the latent heat of solidification. In Eq. [15], R_c is the local cooling rate, ΔH_V is the melting enthalpy (J/kg), κ is the Boltzmann constant, and A is the nucleation morphology index (the spherical nucleus is $3/16\pi$). Therefore, in order to discuss the influence of the cooling rate on the size of AlN during the solidification of steel, we have calculated and discussed the growth of AlN at three cooling rates of 1, 5, and 10 K/s.

Since aluminum and nitrogen segregated during the solidification process, when the reaction of aluminum and nitrogen reached equilibrium at the solidification front, AlN inclusions began to precipitate and grow. However, the actual concentration of Al in the residual liquid phase during the solidification process is far

greater than the actual concentration of N (as shown in Figure 10). Therefore, the N element is the limiting link for the growth of AlN. In order to describe the growth of AlN, it is assumed that the AlN inclusions are spherical and reach a fixed diffusion state. Each inclusion grows independently without interacting with other inclusions. The diffusion flux of nitrogen is expressed by Eq. [16]:

$$J = \frac{D_N}{r} \frac{\rho_{\text{Fe}}}{100M_N} ([\text{pct N}]_L - [\text{pct N}]_e). \quad [16]$$

In Eq. [16], J is the diffusion flux of nitrogen (mol/m² s), r is the radius of AlN (m), D_N is the diffusion coefficient of nitrogen (as shown in Table III), ρ_{Fe} is the density of liquid steel (7.07 g/cm³), M_N is the relative atomic mass of nitrogen, and $[\text{pct N}]_L$ and $[\text{pct N}]_e$ are the actual concentration of element N in the solidification process and the concentration at equilibrium state, respectively.

The relationship between the diffusion flux of nitrogen and the radius of AlN can be expressed by Eq. [17]:

$$4\pi r^2 M_{\text{AlN}} J \Delta t = \frac{4}{3} \pi \rho_{\text{AlN}} [(r + \Delta r)^3 - r^3]. \quad [17]$$

In Eq. [17], M_{AlN} is the molar mass of AlN (41 g/mol), and ρ_{AlN} is the density of AlN (3.26 g/cm³).

According to Eqs. [16] and [17], the theoretical precipitation radius of AlN inclusions in the solidification front of molten steel can be expressed by Eq. [18]:

$$r \frac{dr}{dt} = \frac{M_{\text{AlN}} \rho_{\text{Fe}}}{100M_{\text{Fe}} \rho_{\text{AlN}}} D_N ([\text{pct N}]_L - [\text{pct N}]_e). \quad [18]$$

The integral of the above formula can be obtained:

$$r = \sqrt{\frac{M_{\text{AlN}} \rho_{\text{Fe}}}{50M_{\text{Fe}} \rho_{\text{AlN}}} D_N ([\text{pct N}]_L - [\text{pct N}]_e) t_f}, \quad [19]$$

$$t_f = \frac{T_1 - T_s}{C_R}. \quad [20]$$

In Eq. [19], M_{Fe} is the molar mass of the melt (56 g/mol), and λ_s in Eq [20]. is the local growth time.

The calculated relationship between the precipitation radius of AlN inclusions and solidification fraction during solidification is shown in Figure 12. By setting different cooling rates and initial nitrogen content, it is found that when the initial nitrogen content is 0.001, 0.0015, and 0.00214 pct, AlN inclusions will be precipitated when the solidification fraction is about 0.93, 0.86, and 0.79, respectively. When $[\text{pct N}]_0 = 0.00214$ and the cooling rate was 1, 5, and 10 K/s, the calculated sizes of AlN inclusions at the end of solidification were 7.38, 3.35, and 2.37 μm , respectively; When $[\text{pct N}]_0 = 0.0015$ and the cooling rate was 1, 5, and 10 K/s, the calculated sizes of AlN inclusions at the end of solidification were 5.71, 2.62, and 1.87 μm , respectively; When $[\text{pct N}]_0 = 0.001$ and the cooling rates were 1, 5, and 10 K/s, the calculated sizes of AlN inclusions at the end of solidification were 3.96, 1.84, and 1.34 μm ,

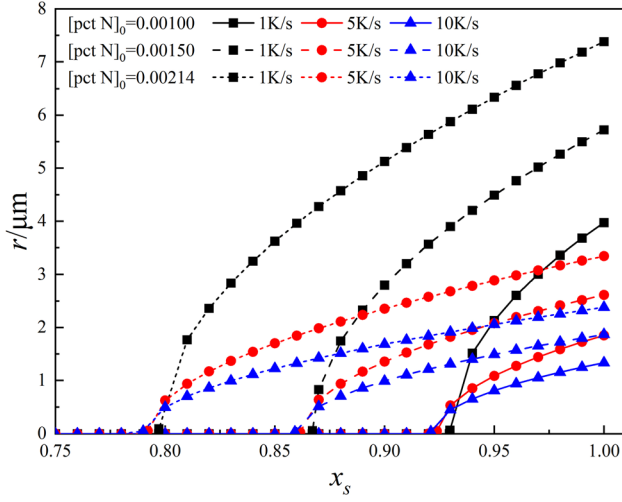
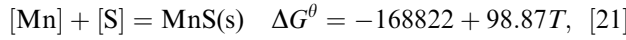


Fig. 12—The relationship between different initial nitrogen content, different cooling rate and solidification fraction and the size of AlN inclusions.

respectively. The calculation results show that the change of cooling rate will lead to the difference of local growth time, which leads to the change of AlN inclusion size with the change of cooling rate. At the same time, under the same cooling rate, the increase in the nitrogen content of the steel will cause the size to increase. Therefore, in industrial production, the size of AlN inclusions can be controlled by reducing the nitrogen content in steel and increasing the cooling rate.

C. Mechanism on the Formation of AlN–MnS Inclusions

AlN–MnS inclusions are common inclusions in high-Al steel, as shown in Figure 5. At 1873 K, the chemical reaction formula formed by MnS inclusions is^[22]



$$\log K'_{\text{MnS}} = \log([\text{pct Mn}] \cdot [\text{pct S}]) = -\frac{8817.9}{T} + 5.15. \quad [22]$$

According to Eqs. [6] through [10], the actual mass percentages of Mn and S elements in the solidification process are calculated, where $k_{\text{Mn}} = 0.77$, $k_{\text{S}} = 0.05$ (as shown in Table IV), the actual solubility product of MnS can be expressed as follows:

$$Q_{\text{MnS}} = C_{\text{L,Mn}} \cdot C_{\text{L,S}}. \quad [23]$$

In Eq. [23] $C_{\text{L,Mn}}$ and $C_{\text{L,S}}$ are the actual mass percentage of element Mn and element S, respectively.

According to Eqs. [22] and [23], the relationship between $\log K'_{\text{MnS}}$, $\log Q_{\text{MnS}}$ and T and x_s can be obtained, as shown in Figure 13. From the intersection of $\log K'_{\text{MnS}}$, and $\log Q_{\text{MnS}}$, it can be seen that MnS precipitates at the solidification end, and the corresponding solidification fraction is about 0.954. Thus, the

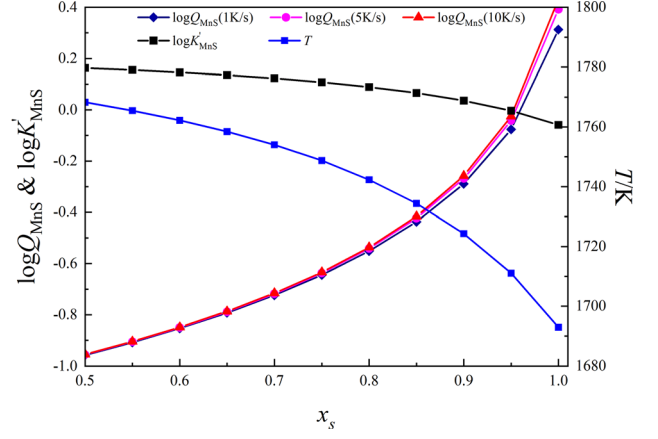


Fig. 13—Precipitation of MnS inclusions during solidification at different cooling rates.

precipitation temperatures of MnS were about 1709.6 K, while the precipitation temperatures of AlN were about 1744 K, which precipitated before MnS. Therefore, it can be considered that AlN inclusions can be used as nucleation sites for MnS heterogeneous nucleation to induce precipitation of MnS and form AlN–MnS inclusions.

Both AlN and MnS are cubic structures and belong to NaCl type crystals. Due to the different atomic distances between AlN and MnS, lattice mismatch will occur when MnS precipitates on the surface of AlN. Therefore, in order to prove that MnS can nucleate the AlN surface, it can be calculated by the two-dimensional mismatch degree proposed by Bramfit.^[35] The two-dimensional mismatch formula is:

$$\delta_{(hkl)_n}^{(hkl)_s} = \frac{1}{3} \left[\sum_{i=1}^3 \frac{|d_{[uvw]_s}^i \cos \theta - d_{[uvw]_n}^i|}{d_{[uvw]_n}^i} \right] \times 100 \text{ pct}. \quad [24]$$

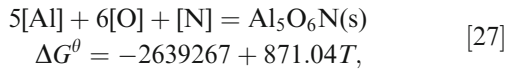
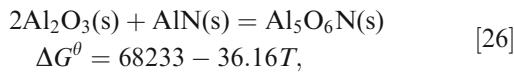
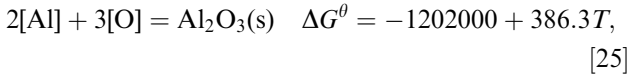
In Eq. [24], $(hkl)_s$ represents a low exponential crystal face on the substrate; $(uvw)_s$ represents a low exponential direction on the crystal plane $(hkl)_s$; $(hkl)_n$ represents a low exponential plane on the nucleating phase; $(uvw)_n$ represents a low exponential direction on the $(hkl)_n$ plane; $d_{[uvw]_s}$ is the distance between atoms in the $(uvw)_s$ direction; $d_{[uvw]_n}$ is the distance between atoms in the $(uvw)_n$ direction; θ is the angle between $(uvw)_s$ and $(uvw)_n$.

Table V shows the crystallographic parameters of various phases.^[36] The two-dimensional mismatch with AlN as the substrate and MnS as the nucleation phase was calculated by Eq. [24]. Table VI shows the calculation results of the lattice mismatch of AlN and MnS at the (100)MnS // (100)AlN, (110)MnS // (110)AlN, and (111)MnS // (111)AlN interfaces, respectively. It can be seen that the mismatch degree of (100)MnS // (100)AlN interface is 8.94 pct, and that of (110)MnS // (110)AlN and (111)MnS // (111)AlN interface are 28.78 pct. Bramfit^[35] believes that when the mismatch rate is less than 12 pct, basal inclusions can be used as effective heterogeneous nucleation sites. Therefore, it can be

shown that AlN and MnS have a higher lattice matching degree at the (100) interface; that is, MnS is easier to nucleate on the (100) plane of AlN inclusions.

D. Thermodynamics of AION Inclusions Precipitation

Park *et al.*^[37] observed single-particle AION inclusions in high-Al steel, and Alba *et al.*^[38] observed AION as Al₂O₃ + AlN multi-phase inclusions. The precipitation behavior of AION inclusions was analyzed by the precipitation rate of AlN in Al₂O₃. However, there is no report on the precipitation behavior of AION single-phase inclusions. AION single-phase inclusions were observed in this study, as shown in Figure 4. Add Eqs. [1], [25], and [26]^[39] to get Eq. [27]:



$$\log K_{\text{Al}_5\text{O}_6\text{N}} = \log(a_{\text{Al}}^5 \cdot a_{\text{O}}^6 \cdot a_{\text{N}}) = -\frac{137841.3}{T} + 45.49. \quad [28]$$

Under the equilibrium conditions of a given temperature, the three-dimensional diagrams of the a(N)-a(O)-a(Al) system under the equilibrium conditions of 1873 K, 1784 K, and 1693 K are drawn according to Eq. [28], as shown in Figures 14(a) through (c). Obviously, AION inclusions can exist stably at this temperature when the activities of Al, N, and O are located above the curved surface but cannot exist stably

Table V. Lattice Parameter Data for AlN and MnS

Inclusion	Crystal System	Lattice Parameter (nm)
AlN	cubic	0.3705
MnS	cubic	0.524 ^[36]

Table VI. Calculation Results of Lattice Mismatch of AlN and MnS

Interface	(100)MnS//(100)AlN			(110)MnS//(110)AlN			(111)MnS//(111)AlN		
	[hkl] _s	[hkl] _n	d[hkl] _s	[hkl] _s	[hkl] _n	d[hkl] _s	[hkl] _s	[hkl] _n	d[hkl] _s
	[001]	[011]	4.069	[001]	[-111]	7.048	[-101]	[-211]	4.984
	[011]	[020]	5.754	[001]	[-110]	5.754	[-101]	[-211]	4.984
	3.705	5.240	3.705	5.240	9.076	7.410	3.705	6.418	3.705
θ (deg)	0			0			0		
Mismatch (δ)	8.94 pct			28.78 pct			28.78 pct		

at this temperature when they are located below the curved surface. In this study, AION inclusions do not precipitate in the liquid and two-phase regions without considering elemental segregation. Therefore, the precipitation behavior of AION inclusions during solidification is further discussed with full consideration of element segregation.

According to Eqs. [6] through [10], the actual mass percentage of Al, O, and N elements in the solidification process are calculated, where $k_{\text{Al}} = 0.6$, $k_{\text{O}} = 0.03$, $k_{\text{N}} = 0.25$ (as shown in Table VI), the actual solubility product of Al₅O₆N can be expressed as follows:

$$\log K_{\text{Al}_5\text{O}_6\text{N}}' = \log([\text{pct Al}]^5 \cdot [\text{pct O}]^6 \cdot [\text{pct N}]) = -\frac{137841.3}{T} + 67.41, \quad [29]$$

$$Q_{\text{Al}_5\text{O}_6\text{N}} = C_{\text{L,Al}}^5 \cdot C_{\text{L,O}}^6 \cdot C_{\text{L,N}}. \quad [30]$$

According to Eq [29]. and [30], the relationship between $\log K'_{\text{AION}}$, $\log Q_{\text{AION}}$ and T and x_s is obtained. As shown in Figure 15, the solidification fraction corresponding to the precipitation of AION inclusions is about 0.96, and the precipitation temperature is about 1707 K. During the solidification process, due to the segregation of Al, O, and N elements, the concentration of each element in the local residual liquid phase increases continuously, exceeding the equilibrium value, the driving force for the formation of AION inclusions increases, and finally AION inclusions are precipitated during the solidification process.

E. Mass Percentage Changes of Inclusions During Solidification

The FToxid, FSstel, and FTmisc databases were used for calculation in FactSage 7.2 software calculation^[27,40-43]. Figure 16 shows the relationship between the mass percentage of inclusions and temperature during solidification (cooling rate of 1 K/s). It is obvious that the inclusions precipitated during solidification are mainly Al₂O₃, AlN, and MnS, which is in good agreement with the inclusion species observed by FESEM-EDS. When the temperature drops from 1873 K to 1784 K (T_1), the inclusions are mainly Al₂O₃ and no MnO and SiO₂ are formed. The reason may be that Fe-Mn and Fe-Si alloys are added first in the alloying process to generate MnO and SiO₂ inclusions. After aluminum is added, MnO and SiO₂ will

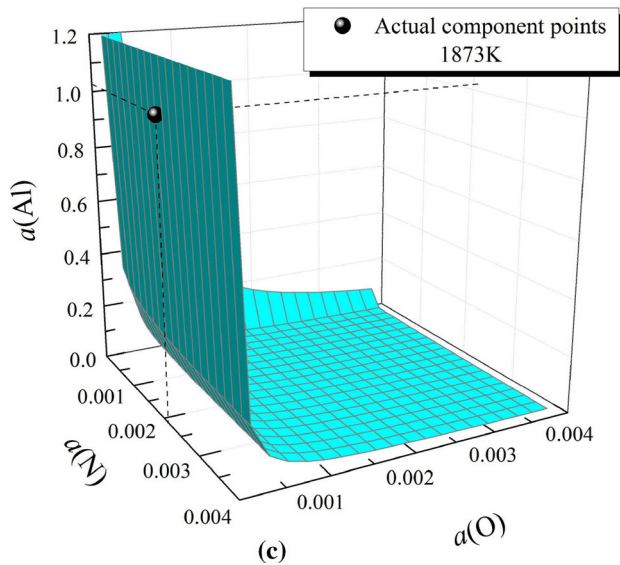
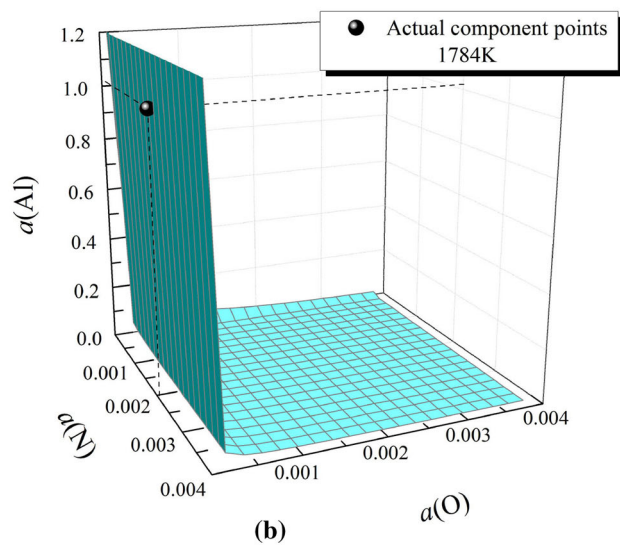
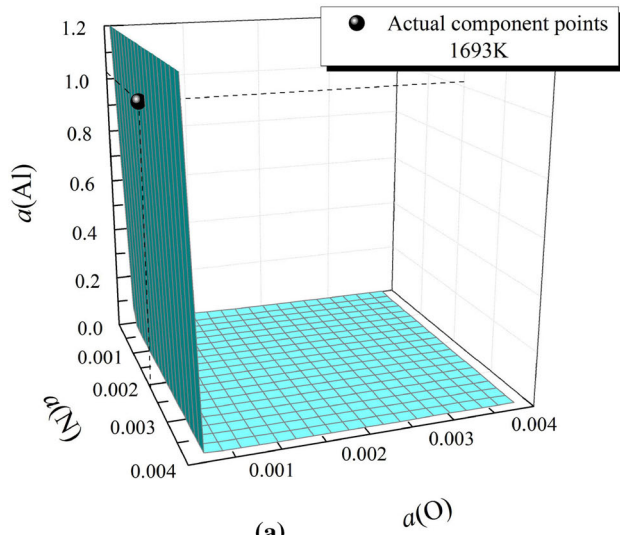


Fig. 14—The stability graph of AlON inclusions is formed under different temperature conditions. (a) 1693 K; (b) 1784 K; (c) 1873 K.

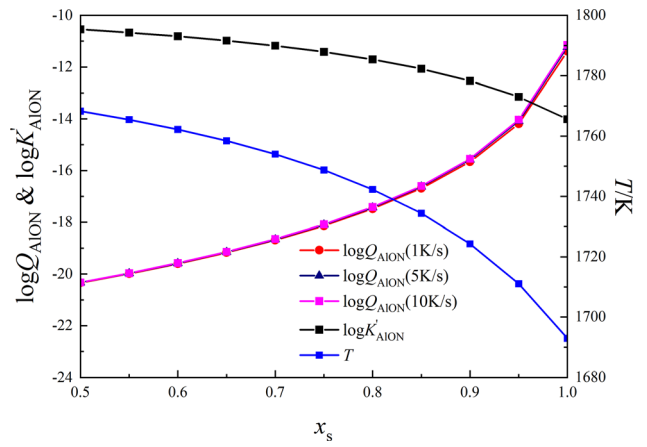


Fig. 15—Precipitation of AlON inclusions during solidification at different cooling rates.

react with Al to form Al_2O_3 inclusions and exist in the molten steel. When the temperature is lowered from 1784 K (T_1) to 1693 K (T_s), AlN and MnS precipitate at 1735 K and 1712 K, respectively, and the corresponding solidification fractions during precipitation are 0.847 and 0.947. After 1693 K (T_s), the precipitation amount of Al_2O_3 , AlN, and MnS inclusions tends to be saturated with the decrease of temperature.

V. CONCLUSIONS

Through the experimental and theoretical calculations studies on the precipitation of AlN inclusions in high-Al steel, the following conclusions can be drawn:

1. FESEM-EDS observation shows that there are single-particle AlN, multi-particle aggregated AlN, AlON, AlN–MnS, and Al_2O_3 –AlN–MnS inclusions in experimental steel. The single-particle AlN inclusions are mainly block and strip, with a size of 1 to 5 μm . The aggregated AlN inclusions are polygonal, annular, and irregular, with sizes ranging from 1 to 13 μm . The size of AlN–MnS and Al_2O_3 –AlN–MnS inclusions is less than 15 μm .
2. The AlN inclusions are precipitated in the two-phase region in the current high-aluminum steel. Growth kinetics shows that increasing the cooling rate and controlling the nitrogen content are beneficial to control the growth of AlN. When the cooling rate is 1 to 10 K/s and the nitrogen content is 0.001, 0.0015, and 0.00214 pct, and the size range of AlN inclusions at the end of solidification is 1.34 to 3.96, 1.87 to 5.71 μm , and 2.37 to 7.38 μm , respectively. In addition, when AlN begins to precipitate, the actual concentration of aluminum is much greater than that of nitrogen. The growth of AlN is considered to be controlled by the diffusion of nitrogen.
3. Thermodynamic calculation shows that the precipitation temperature of MnS inclusions (1709 K) is lower than that of AlN inclusions (1744 K). The mismatch degree of AlN–MnS interface indicates that AlN can provide heterogeneous nucleation sites

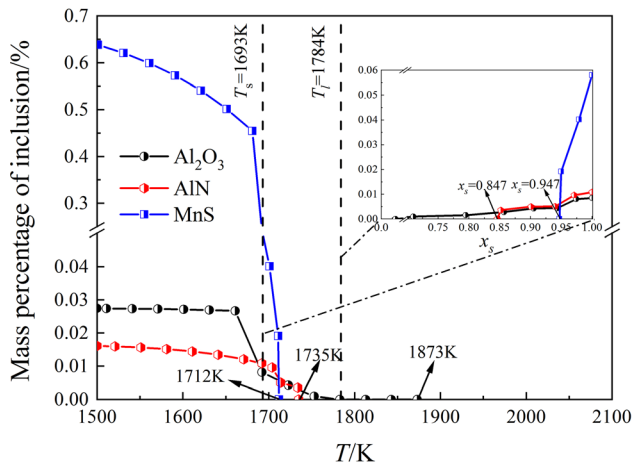


Fig. 16—The relationship between the mass percentage of inclusions and the temperature during the solidification of steel.

for MnS, while MnS can nucleate on (100) plane of AlN, AlN–MnS inclusions can be formed.

- The established $\log K_{\text{AlON}} = -137841.3/T + 45.49$ is used to describe the precipitation of single-phase AlON inclusions. Thermodynamic calculations show that AlON inclusions are precipitated in a two-phase region.
- The types and percentage of inclusions are calculated based on the microsegregation model combined with the FactSage software. The result shows that the inclusions precipitated during solidification are mainly Al_2O_3 , AlN, and MnS, which is in good agreement with the observed inclusions.

ACKNOWLEDGMENTS

The authors are grateful to the National Natural Science Foundation of China (Grant Nos. 52174318 and 51874170) for supporting this work.

CONFLICT OF INTEREST

There are no conflicts to declare.

REFERENCES

- A.S. Hamada, L.P. Karjalainen, and M.C. Karjalainen: *Mater. Sci. Eng. A.*, 2007, vol. 467, pp. 114–24.
- G. Frommeyer and U. Brück: *Steel Res. Int.*, 2006, vol. 77, pp. 627–33.
- G. Frommeyer, U. Brück, and P. Neumann: *ISIJ Int.*, 2003, vol. 43, pp. 438–46.
- I. Gutierrez-Urrutia and D. Raabe: *Acta Mater.*, 2012, vol. 60, pp. 5791–5802.
- C.L. Zhuang, J.H. Liu, Z.L. Mi, H.T. Jiang, D. Tang, and G.X. Wang: *Steel Res. Int.*, 2014, vol. 85, pp. 1432–39.
- Y.N. Wang, J. Yang, R.Z. Wang, X.L. Xin, and L.Y. Xu: *Metall. Mater. Trans. B.*, 2016, vol. 47, pp. 1697–1712.
- H.B. Yin: *Iron Steel Technol.*, 2006, vol. 3, pp. 64–73.
- P. Kaushik, M. Lowry, H. Yin, and H. Pielot: *Ironmak. Steelmak.*, 2012, vol. 39, pp. 284–300.
- H.B. Liu, J.H. Liu, S.K. Michellic, S.B. Shen, X.F. Su, B.W. Wu, and H. Ding: *Steel Res. Int.*, 2016, vol. 87, pp. 1723–32.

- M. Vedani, D. Dellasega, and A. Mannucci: *ISIJ Int.*, 2009, vol. 49, pp. 446–52.
- M. Alba, M. Nabeel, and N. Dogan: *Steel Res. Int.*, 2019, vol. 91, p. 1900477.
- M.K. Paek, J.M. Jang, and K.H.J.J. DoPak: *Met. Mater. Int.*, 2013, vol. 19, pp. 1077–81.
- S.E. Kang, J.R. Banerjee, A. Tuling, and B. Mintz: *Mater. Sci. Technol.*, 2014, vol. 30, pp. 1328–35.
- G.D. Funnell and R.J. Davies: *Met. Technol.*, 1978, vol. 5, pp. 150–53.
- N.H. Croft, A.R. Entwisle, and G.J. Davies: *Met. Technol.*, 1983, vol. 10, pp. 125–29.
- C.B. Shi, X.C. Chen, and H.J. Guo: *Int. J. Miner. Metall. Mater.*, 2012, vol. 19, pp. 19–26.
- H.B. Liu, J. Liu, S. Michellic, F. Wei, C. Zhuang, Z. Han, and S. Li: *Ironmak. Steelmak.*, 2016, vol. 43, pp. 171–79.
- Y.N. Wang, J. Yang, X.L. Xin, R.Z. Wang, and L.Y. Xu: *Metall. Mater. Trans. B.*, 2016, vol. 47B, pp. 1378–89.
- M. Nabeel, M. Alba, and N. Dogan: *Crystals*, 2020, vol. 10, p. 1054.
- M.K. Paek, J.M. Jang, H.J. Kang, and J.J. Pak: *ISIJ Int.*, 2013, vol. 53, pp. 535–37.
- D.H. Kim, M.S. Jung, H. Nam, M.K. Paek, and J.J. Pak: *Metall. Mater. Trans. B.*, 2012, vol. 43B, pp. 1106–12.
- G.K. Sigworth and J.F. Elliott: *Met. Sci.*, 1974, vol. 8, pp. 298–310.
- M.K. Paek, J.M. Jang, M. Jiang, and J.J. Pak: *ISIJ Int.*, 2013, vol. 53, pp. 973–78.
- H. Itoh, M. Hino, and S. Ban-ya: *Tetsu-to-Hagané.*, 1997, vol. 83, pp. 773–78.
- H. Wada and R.D. Pehlke: *Metall. Mater. Trans. B.*, 1978, vol. 9B, pp. 441–48.
- T.W. Clyne and W. Kurz: *Metall. Mater. Trans. A.*, 1981, vol. 12A, pp. 965–71.
- S.K. Choudhary and A. Ghosh: *ISIJ Int.*, 2009, vol. 49, pp. 1819–27.
- Y.M. Won and B.G. Thomas: *Metall. Mater. Trans. A.*, 2001, vol. 32A, pp. 1755–67.
- L. Cao, G.C. Wang, Y.Y. Xiao, and R.G. Yang: *J. Iron Steel Res. Int.*, 2022, vol. 9, pp. 925–38.
- L. Cao, G.C. Wang, X.H. Yuan, P.L. Jin, and S. Sridhar: *Metals.*, 2019, vol. 9, p. 900.
- K. Sasai: *ISIJ Int.*, 2016, vol. 56, pp. 1013–22.
- W.S. Wang, H.Y. Zhu, Y. Han, J.L. Li, and Z.L. Xue: *Ironmak. Steelmak.*, 2021, vol. 48, pp. 1038–47.
- H.B. Liu, J.H. Liu, S. Michellic, S.B. Shen, B.W. Wu, and H. Ding: *Steel Res. Int.*, 2016, vol. 87, pp. 1723–32.
- E.Z. Gao, G. Zou, W.L. Wang, F.J. Ma, and X.C. Luo: *Metall. Mater. Trans. B.*, 2017, vol. 48B, pp. 1014–23.
- B.L. Bramfitt: *Metall. Trans.*, 1970, vol. 1, pp. 1987–95.
- H. Ott: *Z. Krist. Cryst. Mater.*, 1926, vol. 63, pp. 222–30.
- J.H. Park, D.J. Kim, and J.M. Dong: *Metall. Mater. Trans. B.*, 2012, vol. 43, pp. 2316–24.
- M. Alba, M. Nabeel, and N. Dogan: *Ironmak. Steelmak.*, 2020, vol. 48, pp. 379–86.
- Y.Z. Wang, T.C. Lu, Y. Yu, J.Q. Qi, J.S. Wen, H.P. Wang, L. Xiao, Z.L. Yang, J. Yu, Y. Wen, and N. Wei: *Rare Met. Mater. Eng.*, 2009, vol. 38, pp. 48–51.
- L. Cao, D.L. Shang, X.G. Ai, P.L. Jin, Y.Y. Xiao, G.C. Wang, and C.W. Liu: *J. Iron Steel Res. Int.*, 2021, vol. 28, pp. 402–12.
- C.S. Liu, D. Kumar, B.A. Webler, and P.C. Pistorius: *Metall. Mater. Trans. B.*, 2020, vol. 51B, pp. 529–42.
- S.P. Piva, D. Kumar, and P.C. Pistorius: *Metall. Mater. Trans. B.*, 2017, vol. 48B, pp. 37–45.
- J.D. Steenkamp, P.C. Pistorius, and M. Tangstad: *Metall. Mater. Trans. B.*, 2015, vol. 46B, pp. 653–67.

Publisher's Note Springer Nature remains neutral with regard to jurisdictional claims in published maps and institutional affiliations.

Springer Nature or its licensor (e.g. a society or other partner) holds exclusive rights to this article under a publishing agreement with the author(s) or other rightsholder(s); author self-archiving of the accepted manuscript version of this article is solely governed by the terms of such publishing agreement and applicable law.